# Frequent Floods in the Yangtze River Basin Linked to a shifted Indian Ocean Wave Regime

Panini Dasgupta[1], SungHyun Nam[1,2,3*], Michael J. McPhaden[4*], Dong-Jin Kang[5,6], M. K. Roxy[7], Saranya. J. S.[1]

[1]*Future Innovation Institute, Seoul National University, Siheung 15011, Republic of Korea*

[2]*School of Earth and Environmental Sciences, College of Natural Sciences, Seoul National University, Seoul, Republic of Korea*

[3]*Research Institute of Oceanography, College of Natural Sciences, Seoul National University, Seoul, Republic of Korea*

[4]*Pacific Marine Environmental Laboratory, National Oceanic and Atmospheric Administration, Seattle, WA, USA*

[5]*Department of Ocean Science, University of Science and Technology, Daejeon, Republic of Korea*

[6]*Office of the Vice President, Korea Institute of Ocean Science and Technology, Busan, Republic of Korea*

[7]*Centre for Climate Change Research, Indian Institute of Tropical Meteorology, Ministry of Earth Sciences, Pune, India*

[*]**Corresponding authors**:

SungHyun Nam

School of Earth and Environmental Sciences, Seoul National University

Seoul 08826, South Korea

namsh@snu.ac.kr

Michael J. McPhaden

Pacific Marine Environmental Laboratory, National Oceanic and Atmospheric Administration

Seattle, WA, USA

michael.j.mcphaden@noaa.gov

## Supplementary Materials

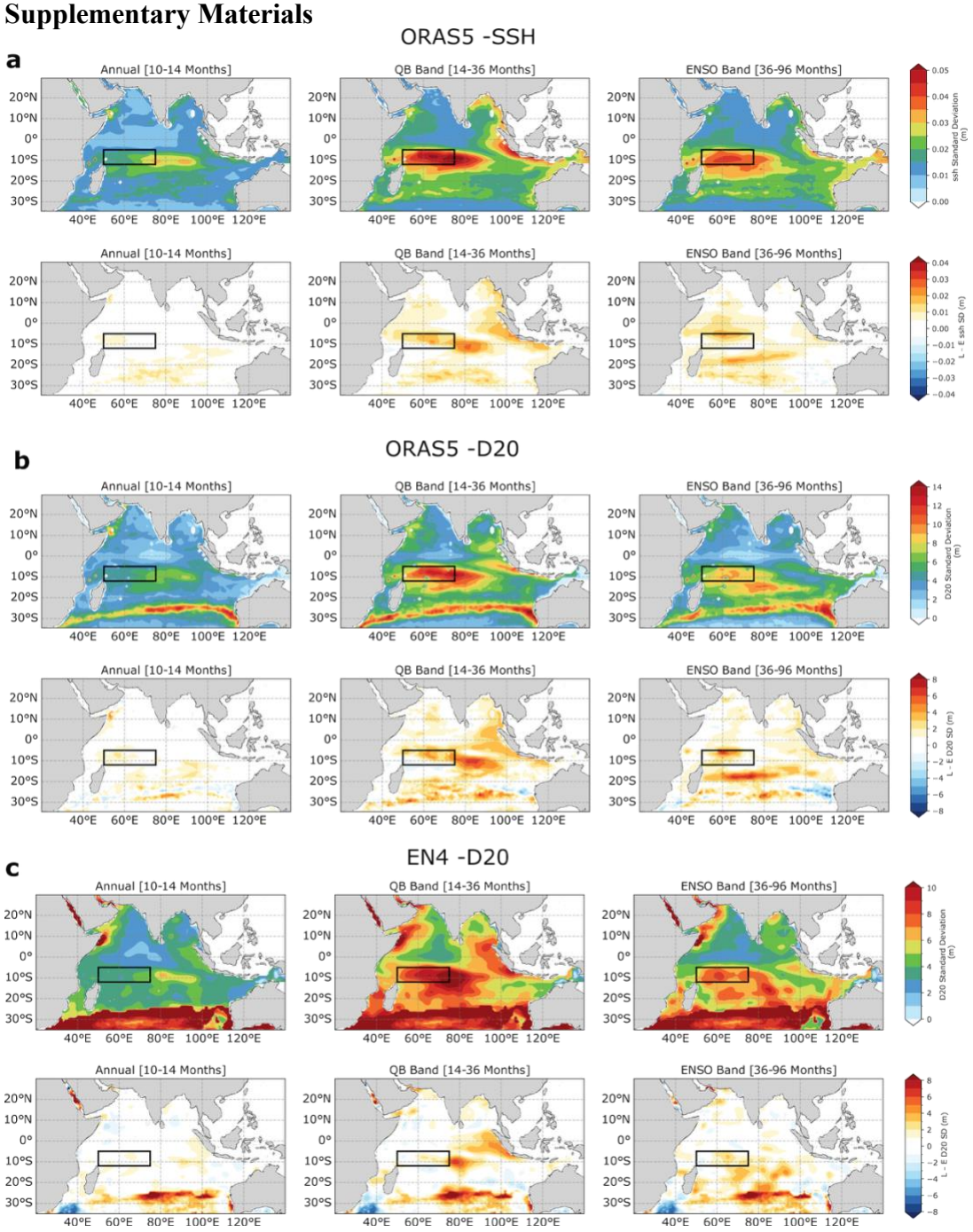


**Supplementary Fig. 1** | Variability of **(a)** ORAS5 SSH [m], **(b)** ORAS5 D20 [m], and **(c)** EN4 D20 [m] anomalies across three frequency bands: annual (10–14 months), quasi-biennial (QB) (14–36 months), and low-frequency (ENSO band) (36–96 months), after removal of the seasonal cycle. The upper panels show the standard deviation for each band, while the lower panels display the change in standard deviation between the Early (1960–1991) and Late (1992–2024) periods.

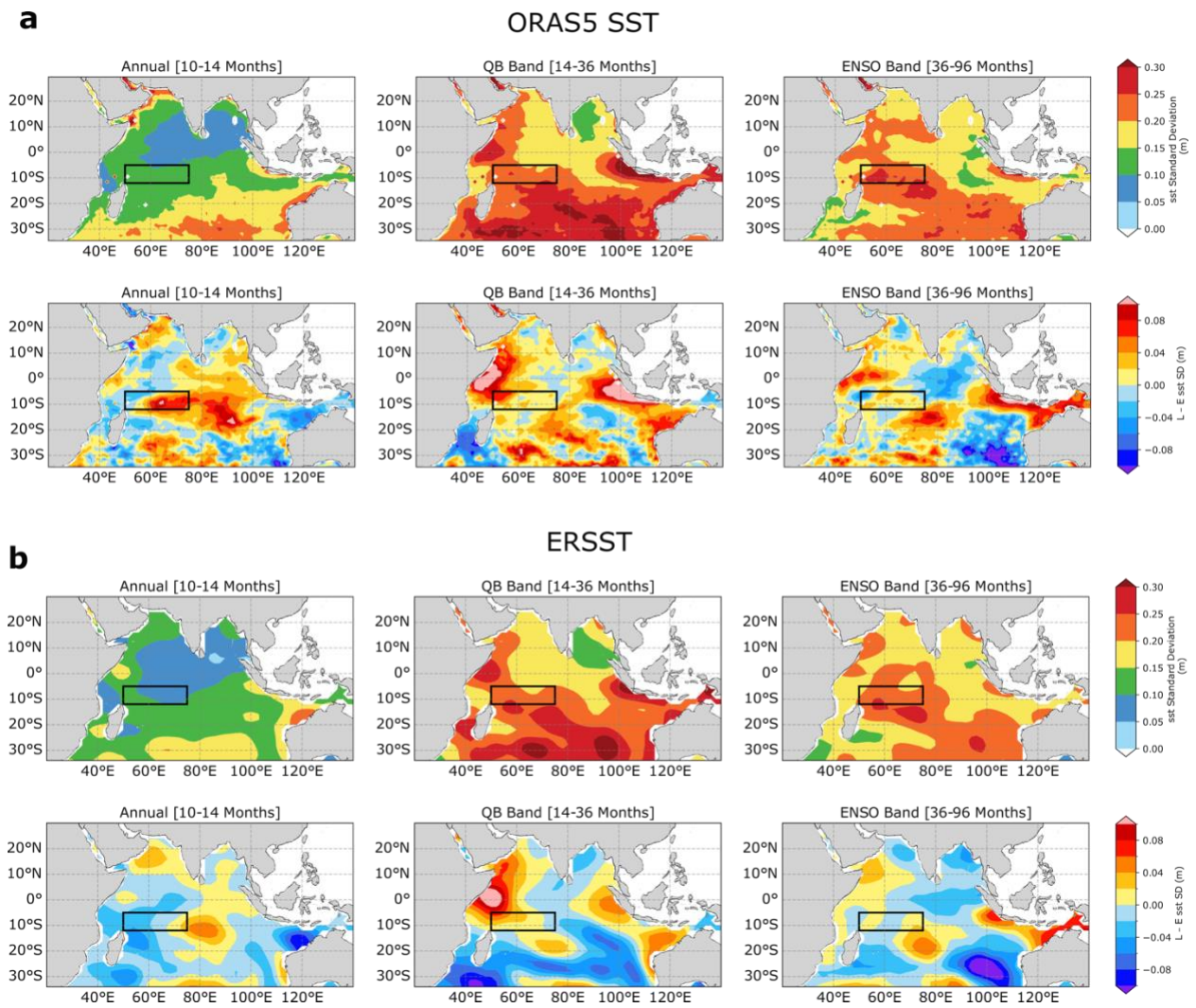


**Supplementary Fig. 2** | Variability of **(a)** ORAS5 SST [°C], **(b)** ERSST [°C], anomalies across three frequency bands: annual (10–14 months), quasi-biennial (QB) (14–36 months), and low-frequency (ENSO band) (36–96 months), after removal of the seasonal cycle. The upper panels show the standard deviation for each band, while the lower panels display the change in standard deviation between the Early (1960–1991) and Late (1992–2024) periods.

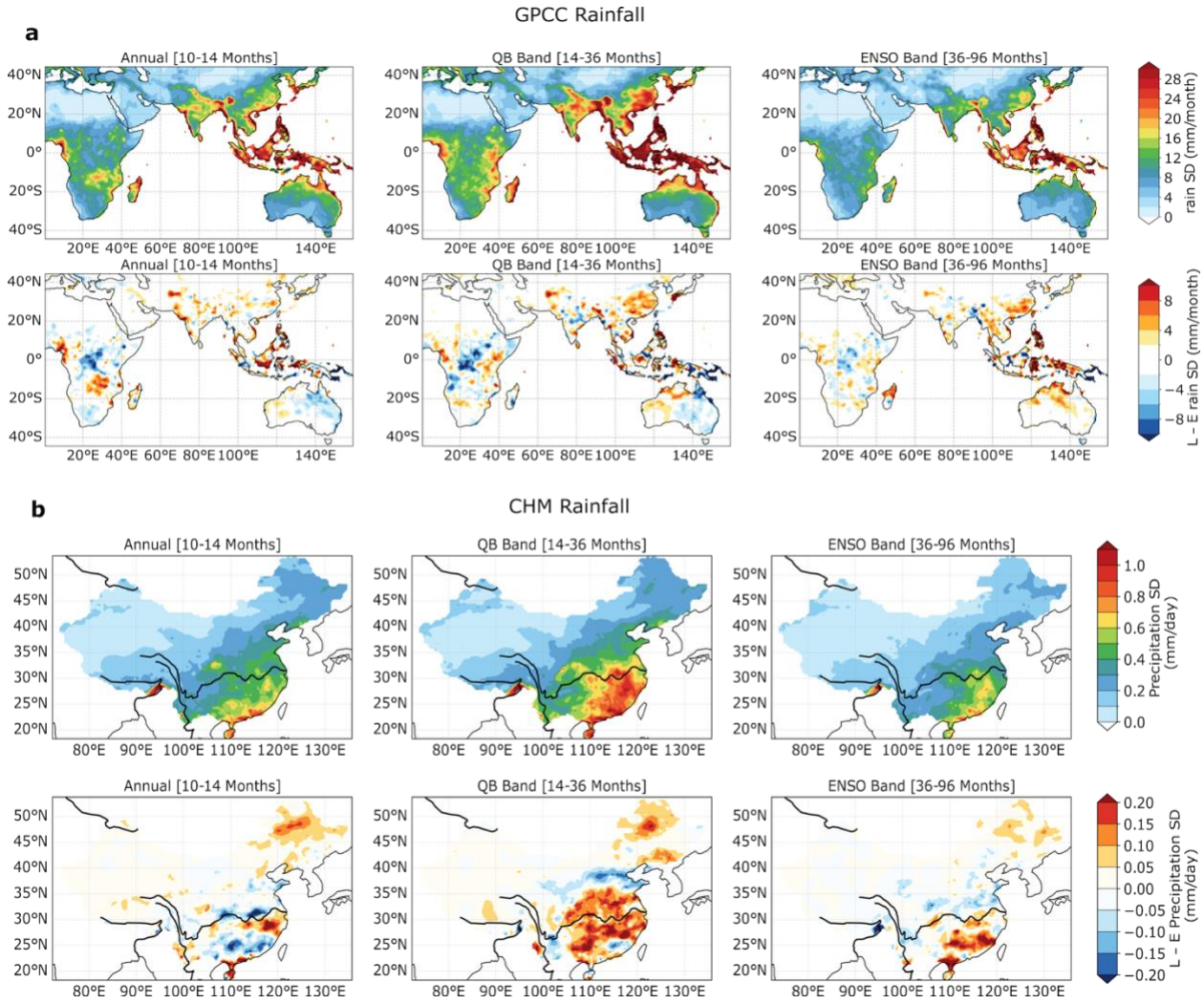


**Supplementary Fig. 3** | Variability of **(a)** GPCC rainfall [mm/month], **(b)** CHM rainfall [mm/day], anomalies across three frequency bands: annual (10–14 months), quasi-biennial (QB) (14–36 months), and low-frequency (ENSO band) (36–96 months), after removal of the seasonal cycle. The upper panels show the standard deviation for each band, while the lower panels display the change in standard deviation between the Early (1960–1991) and Late (1992–2024) periods.

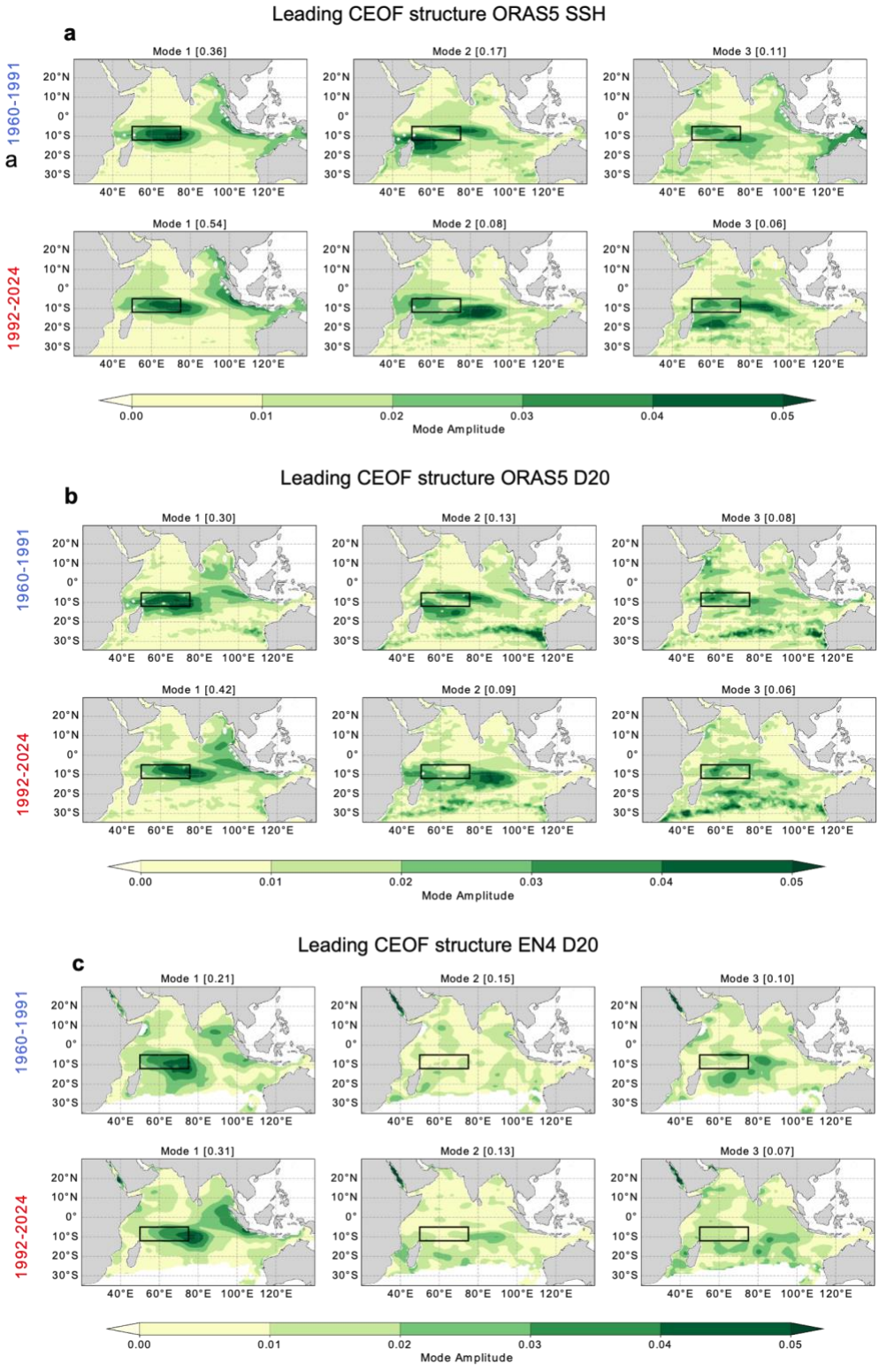


**Supplementary Fig. 4** | Amplitudes of the leading three Complex Empirical Orthogonal Function (CEOF) modes during the Early (1960–1991) and Late (1992–2024) periods, derived from **(a)** ORAS5 SSH [m], **(b)** ORAS5 D20 [m], and **(c)** EN4 D20 [m].

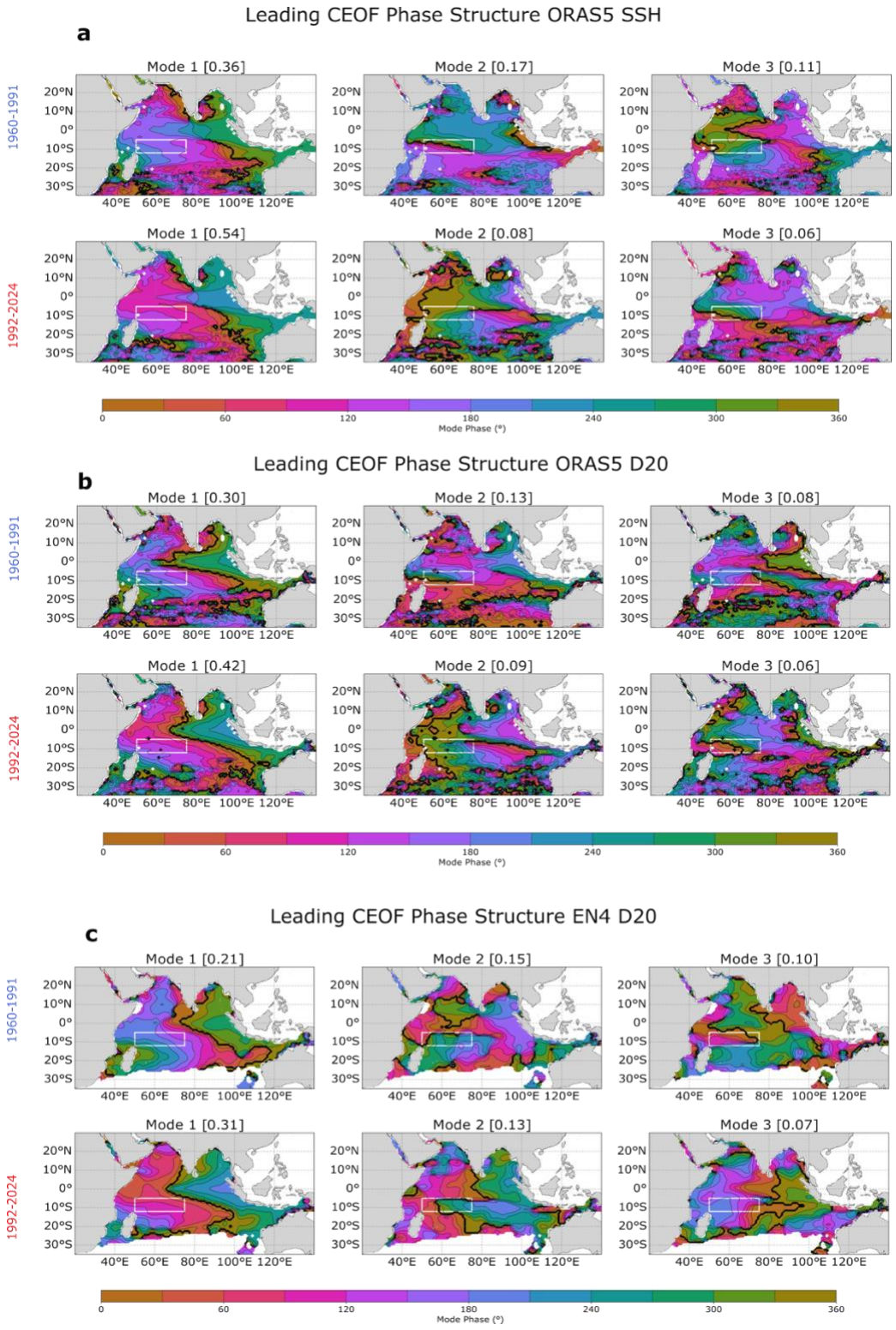


**Supplementary Fig. 5 |.** Phases of the leading three Complex Empirical Orthogonal Function (CEOF) modes during the Early (1960–1991) and Late (1992–2024) periods, derived from **(a)** ORAS5 SSH [m], **(b)** ORAS5 D20 [m], and **(c)** EN4 D20 [m].

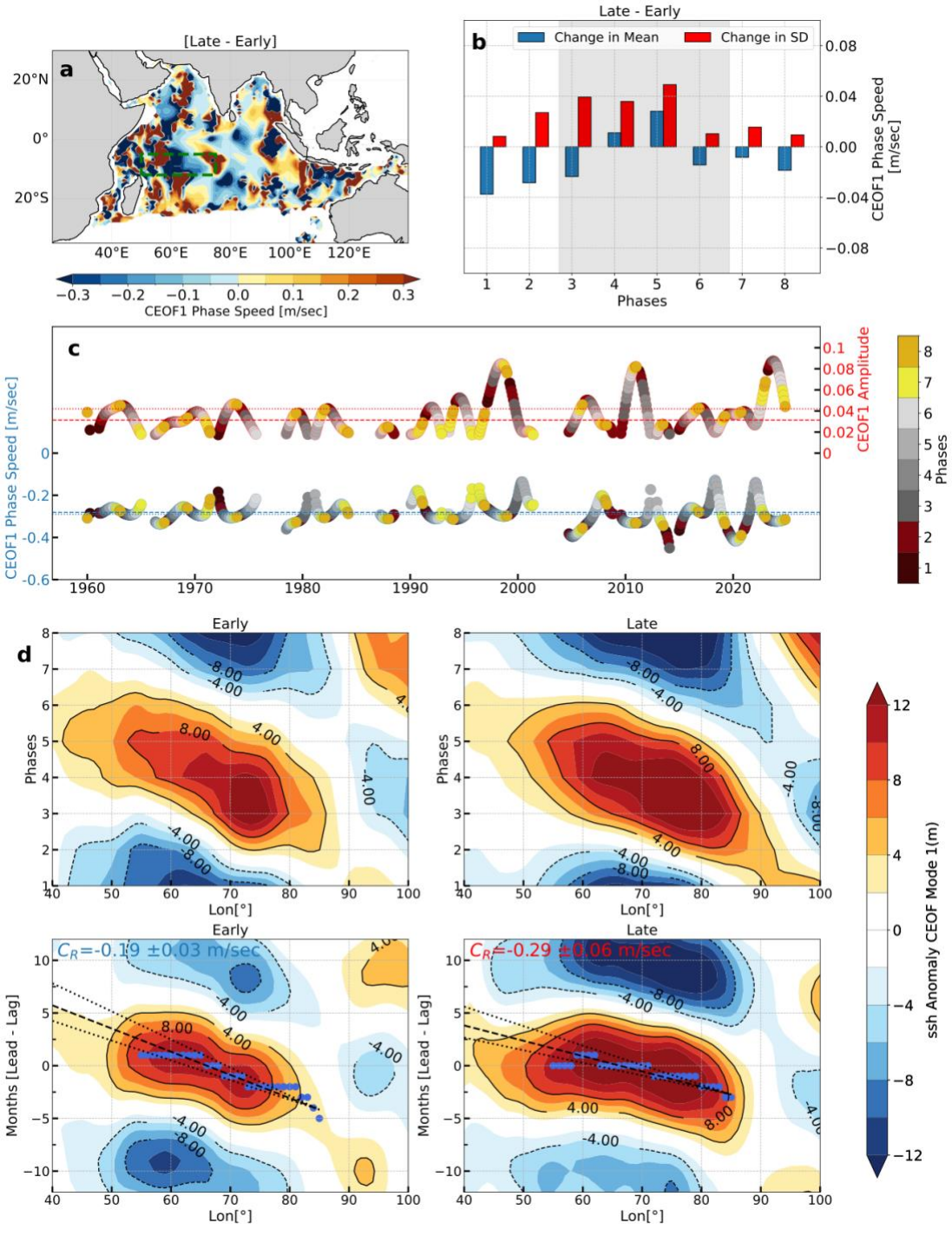


**Supplementary Fig. 6 | Changes in the westward phase speed of baroclinic Rossby Waves evident in the first complex EOF mode. (a)** Change in the phase speed of the first CEOF mode of QB–D20 EN4 [m/sec] between the Late [1992–2024] and Early [1960–1991] periods. **(b)** Change in the mean and standard deviation of westward phase speed over the SCTR across eight CEOF phases. Phase speeds were calculated based on the spatial phase structure averaged over

the SCTR and temporal phase evolution, using the full-period [1960–2024] mean. **(c)** Time series of phase speed over the SCTR and amplitude of the first CEOF mode. **(d) (Top)** Hovmöller plot showing longitudinal propagation of QB-D20 EN4 [m] anomalies averaged between 5°S–12°S across eight CEOF phases during the Early and Late periods. **(Bottom)** Composite lagged propagation of QB-D20 EN4 [m], centred on anomalous peaks (exceeding one standard deviation) over the SCTR.

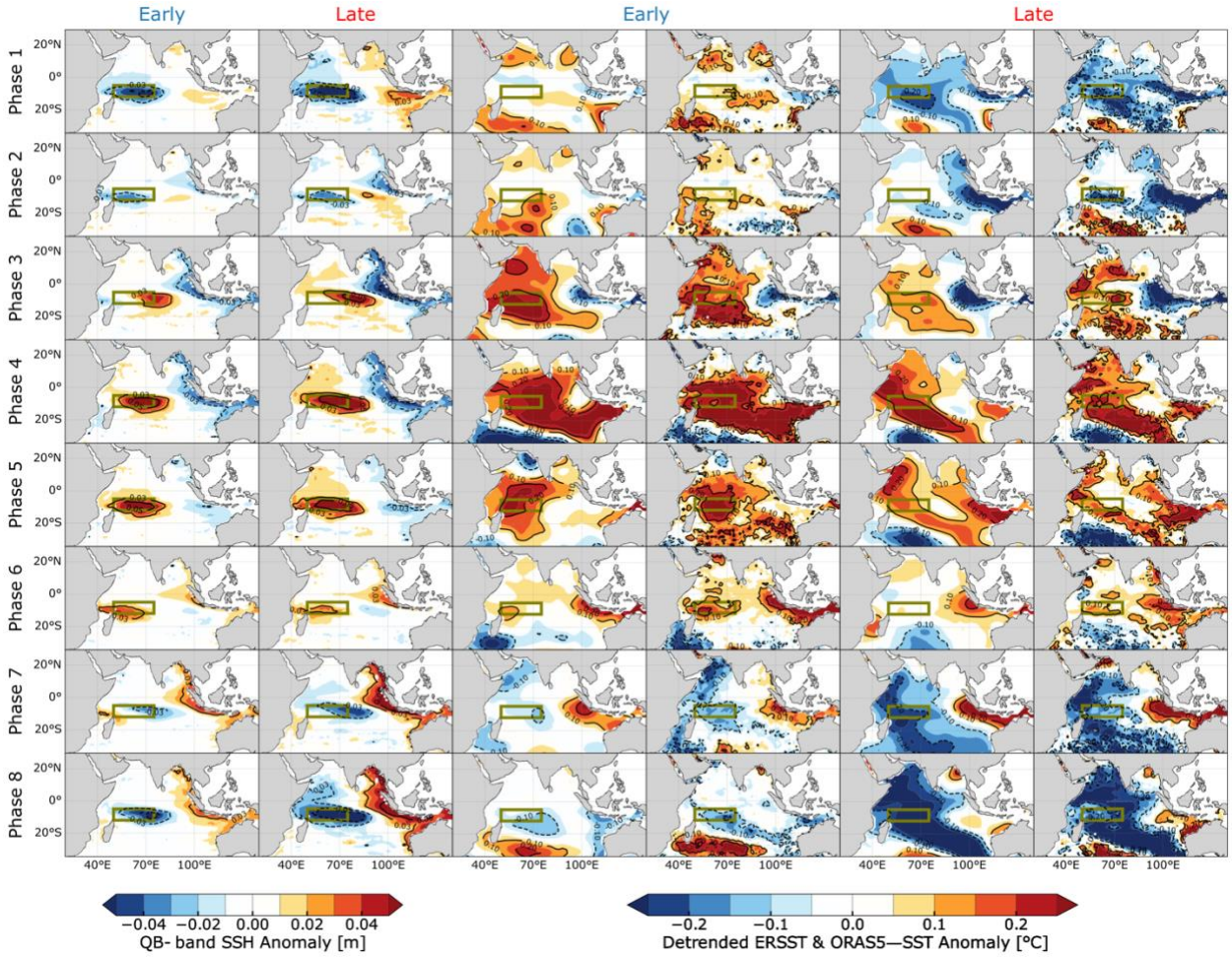


**Supplementary Fig. 7 | CEOF phase composites of QB-SSH, detrended ERSST, and detrended ORAS5-SST during Early and Late periods.**

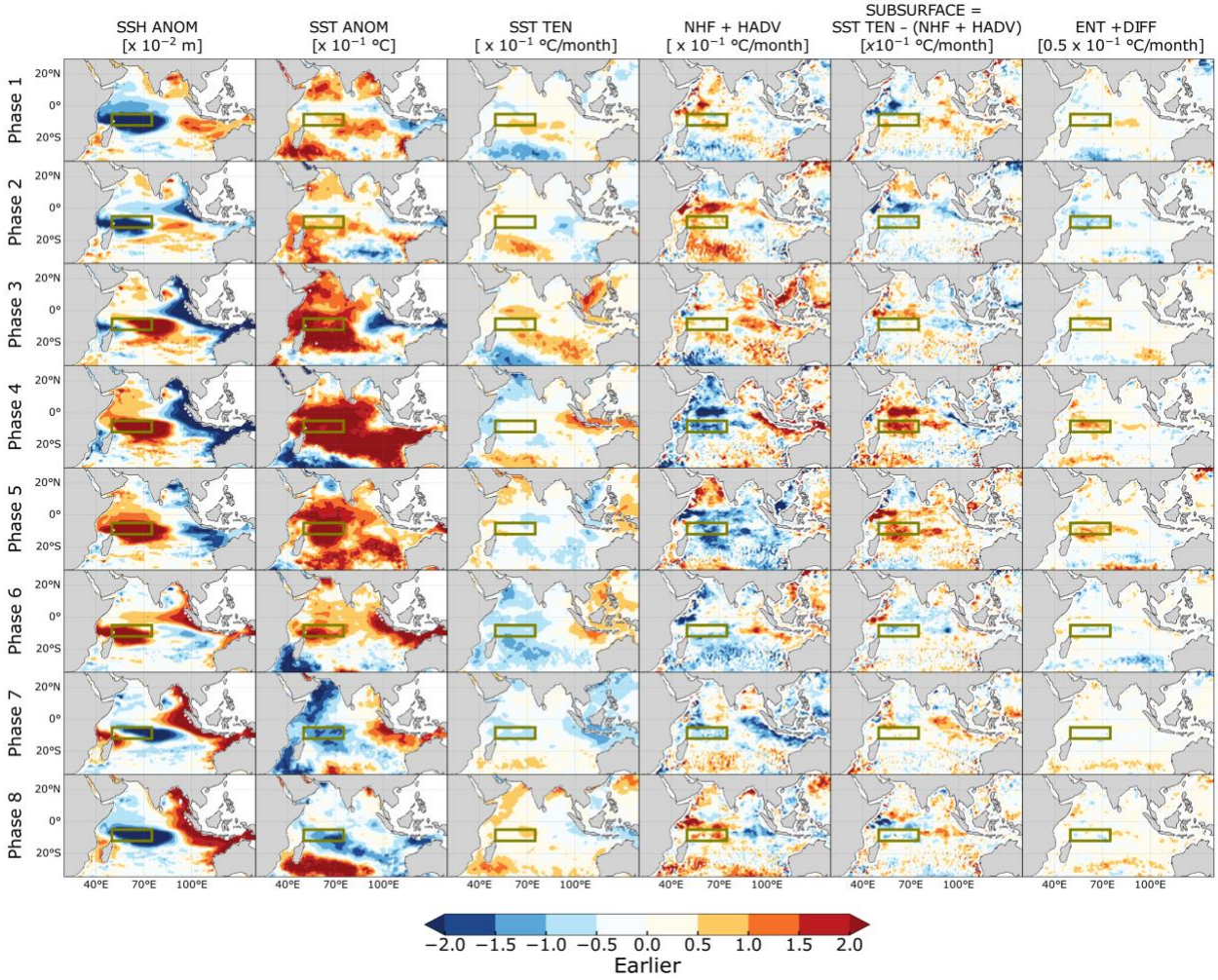


**Supplementary Fig. 8 | Early CEOF phase composites of SSH, SST, and surface mixed layer heat balance.** Each column (from left to right) represents the mean field in active CEOF1 phases during the Early Period. The variables shown include 1. QB-SSH anomalies [m], 2. Detrended SST anomalies [°C], detrended anomalies of mixed layer heat balance terms: 3. SST tendencies [°C/month], 4. Net surface heat flux plus horizontal heat advection [°C/month], representing surface mixed layer processes (based on a 0.03 kg/m³ density criterion for the mixed layer), 5. Unresolved subsurface processes, inferred as the residual between total temperature tendency and surface mixed layer contributions, 6. Vertical processes, including vertical entrainment and turbulent diffusion terms [°C/month]. The vertical entrainment term is contributed by the entrainment processes due to mixed layer tendency, mixed layer advection, and vertical heat advection.

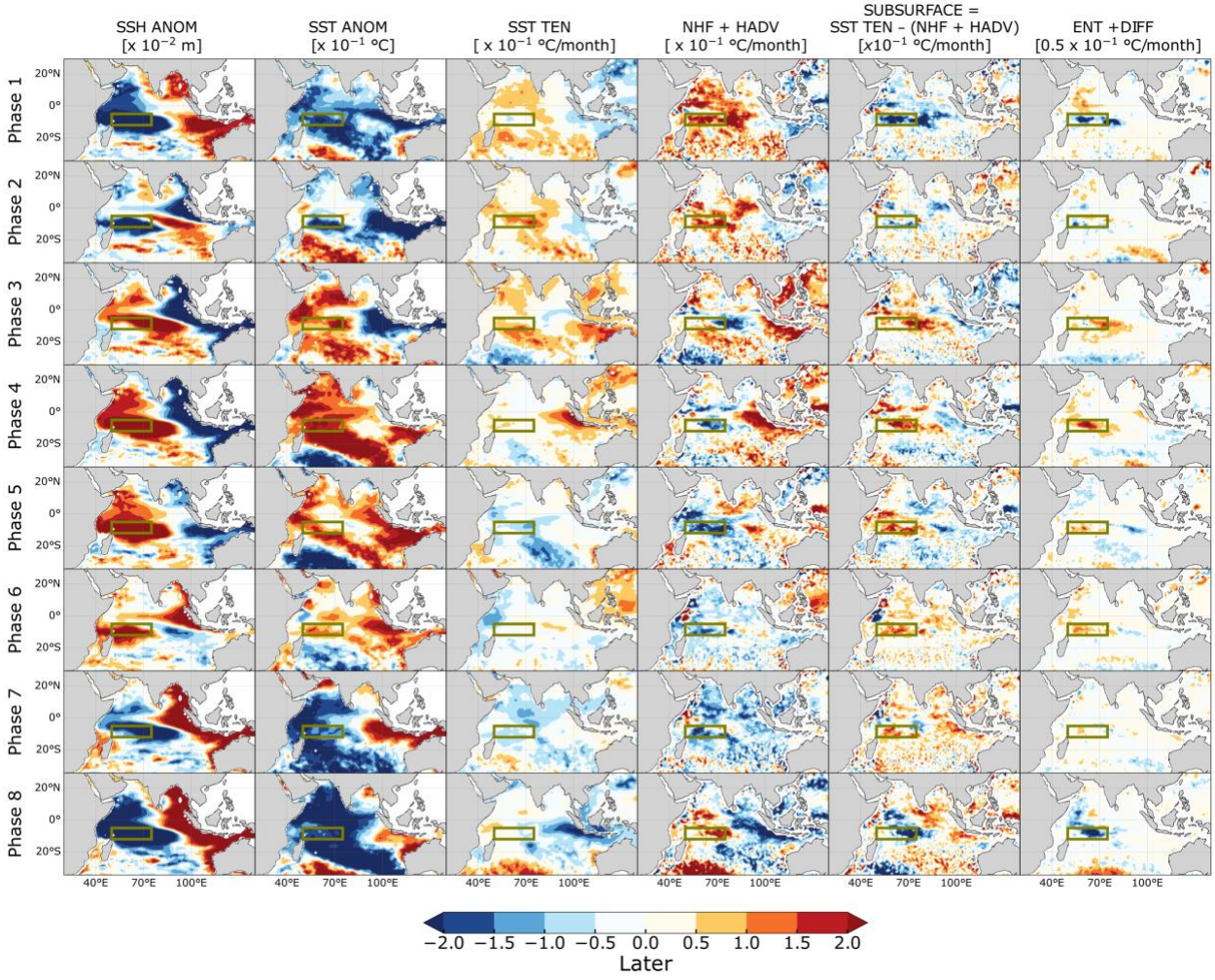


**Supplementary Fig. 9 | Late CEOF phase composites of SSH, SST, and surface mixed layer heat balance.** Same as Supplementary Figure 8 for the Late Period.

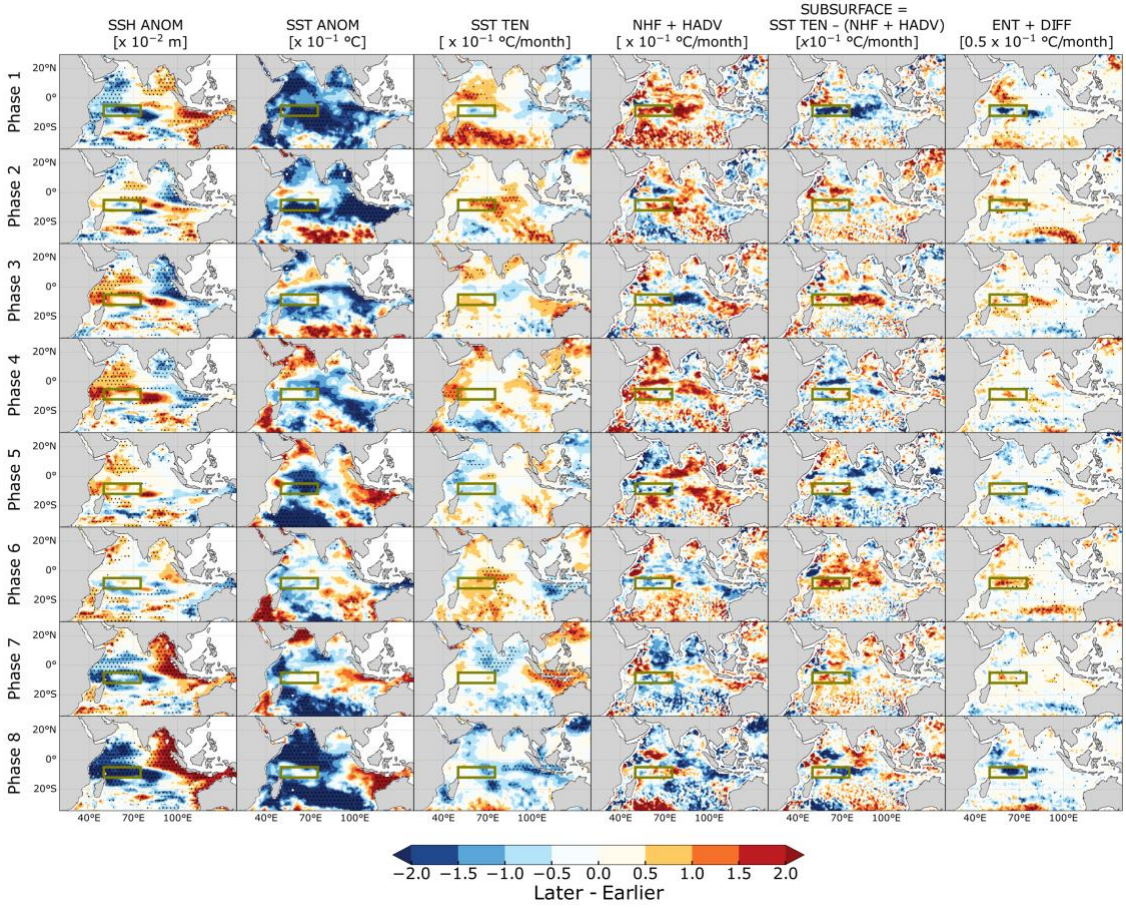


104

105 **Supplementary Fig. 10 | Later–Early CEOF phase composites of SSH, SST, and surface**
106 **mixed layer heat balance.** Each column (from left to right) represents the difference between
107 the Later and Early periods across the eight phases of the CEOF1 mode. The variables shown
108 include 1. QB-SSH anomalies [m], 2. Detrended SST anomalies [°C], detrended anomalies of
109 mixed layer heat balance terms: 3. SST tendencies [°C/month], 4. Net surface heat flux plus
110 horizontal heat advection [°C/month], representing surface mixed layer processes (based on a
111 0.03 kg/m³ density criterion for the mixed layer), 5. Unresolved subsurface processes—inferred
112 as the residual between total temperature tendency and surface mixed layer contributions, 6.
113 Vertical processes, including vertical entrainment and turbulent diffusion term [°C/month]. The
114 vertical entrainment term is contributed by the entrainment processes due to mixed layer
115 tendency, mixed layer advection, and vertical heat advection. Dots indicate regions where the
116 differences are statistically significant ($p < 0.05$), based on a two-sample *t*-test.

117

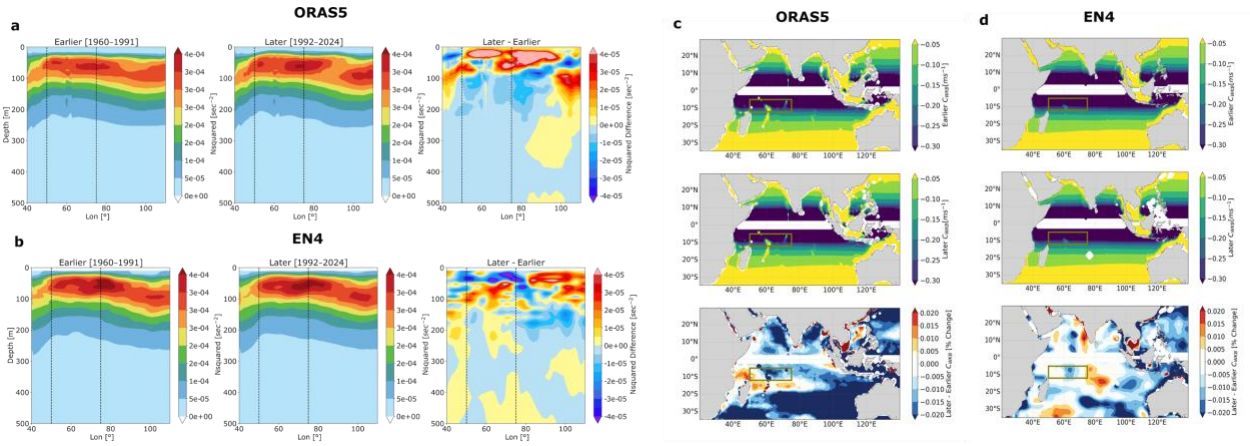


**Supplementary Fig. 11 | Mean stratification changes between Early and Late periods and associated changes in the free first-mode baroclinic Rossby wave phase speed calculated using WKBJ approximation.** Stratification of Early and Late periods and their difference in SCTR latitude 12°S–5°S for (**a**) ORAS5 and (**b**) EN4. Corresponding free first-mode baroclinic Rossby wave phase speed for (**c**) ORAS5 and (**d**) EN4.

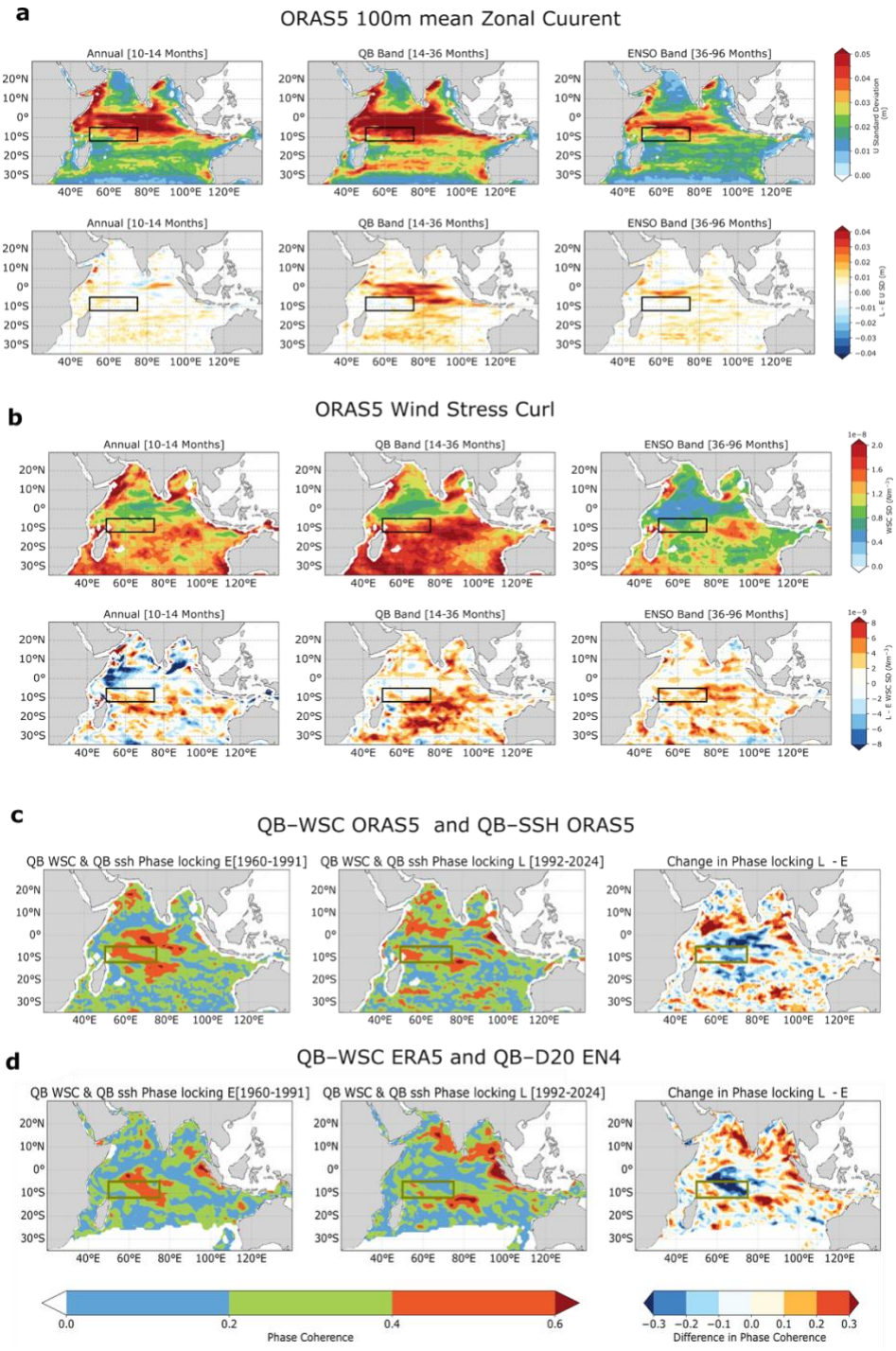


**Supplementary Fig. 12** | Variability of **(a)** ORAS5 upper 100-m mean zonal current [m $s^{-1}$] and **(b)** wind stress curl (N $m^{-3}$) anomalies across three frequency bands: annual (10–14 months), quasi-biennial (QB) (14–36 months), and low-frequency (ENSO band) (36–96 months), after removal of the seasonal cycle. The upper panels show the standard deviation for each band, while the lower panels display the change in standard deviation between the Early (1960–1991) and Late (1992–2024) periods. (**c**) Phase coherence between QB band ORAS5 wind stress curl

and ORAS5 SSH. (**d**) Phase coherence between QB band ERA5 wind stress curl and QB band EN4 D20. Early, Late and their differences.

### 1.1 Faster wave propagation and associated mixed layer heat imbalance

In the main article, we demonstrated mean acceleration of the Kelvin–Rossby wave cycle during the Late period compared with the Early period. However, how this acceleration manifests in the mixed layer heat budget and contributes to the observed increase in the QB variability of SST remains unclear, particularly over the western and eastern poles of the equatorial Indian Ocean, and over the SCTR region. To investigate this, we conducted a monthly ocean surface mixed layer heat budget analysis using a density difference criterion of 0.03 kg $m^{-3}$ to define the surface mixed layer. Supplementary Fig. 7 presents phase composites (based on the CEOF1 amplitude threshold discussed earlier) of QB band SSH and detrended SST anomalies from ERSST and ORAS5 across eight distinct phases, for both Early and Late periods. These composites revealed marked differences in the propagation of QB-SSH anomalies and the corresponding SST response in the two products. To explore the mechanisms underlying these SST responses, we showed the detrended anomalies of the heat budget components in Supplementary Figs. 8 and 9, representing the Early and Late periods, respectively. The methodology for heat budget calculation is detailed in the Methods section. It is important to note that SST tendencies are typically reflected in SST anomalies during the subsequent phases, as seen in Supplementary Figs. 8 and 9. To distinguish between surface and subsurface influences on SST, we categorized the budget terms into three components: **Surface processes**, comprising net surface heat flux and horizontal advection within the mixed layer; **unresolved subsurface processes**, inferred as the residual between total temperature tendency and surface mixed layer contributions; **vertical processes**, including vertical entrainment and turbulent diffusion. As expected, vertical processes accounted for approximately 50% of the unresolved subsurface contribution across most phases. A key finding is that, across nearly all phases, subsurface processes tended to be out of phase with surface processes, particularly over the SCTR region. This compensatory relationship has also been reported in previous mixed-layer heat budget studies over the SCTR. In Figure 4, we present the difference in heat budget terms between the Late and Early periods. A notable feature is the presence of anomalous mixed layer temperature tendencies during CEOF phases 2–7 in the Late period, significantly contributed by subsurface processes. In Phase 6, despite negative

contributions from surface processes, SST tendencies remained anomalously high due to strong subsurface influences. Notably, Phase 6 corresponds to the transition from down- to upwelling Rossby waves in the SCTR region. Additionally, during phases 3 and 4, accelerated Rossby wave propagation and its reflection as Kelvin waves appeared to enhance SST anomalies over the western and eastern equatorial Indian Ocean, respectively. These results provide compelling evidence that the observed QB-SST variability is tightly linked to the evolving nature of underlying tropical wave dynamics.